Dynamics of picosecond-laser-pulse plasmas determined from the spectral shifts of reflected probe pulses

O. L. Landen

*Lawrence Livermore National Laboratory, Livermore, California 94550
and Department of Applied Science, University of California Davis, Davis, California 95616*

W. E. Alley

Lawrence Livermore National Laboratory, Livermore, California 94550

The evolution of density profiles in plasmas produced by 10^{14}-W cm^{-2}, 1-ps, 580-nm-wavelength laser pulses has been determined from spectral shifts imposed on a reflected picosecond probe pulse. The shifts are caused by two mechanisms: hydrodynamic expansion and ionization front motion. Both time-resolved expansion velocities and ionization rates are inferred from the spectral shifts and are compared to one-dimensional hydrodynamic simulations.

I. INTRODUCTION

The interaction of high-intensity picosecond and subpicosecond laser pulses with solid targets is a current topic of great interest [1–19] The resultant plasmas formed have initially extremely steep density gradients. Experimental studies to date on such plasmas have concentrated on linear [1–8] and nonlinear [9] optical properties and ultrashort x-ray pulse generation [3,10–17]. In addition, the promise [20,21] exists for creating uniform, solid- to super-solid-density, high-temperature plasmas for spectroscopic diagnosis. In all cases, the type and degree of laser-plasma coupling is sensitively dependent on the amount of significant (> 1 nm) plasma expansion occurring during and after laser energy deposition. Hence both energy deposition rates [3,5,10–15,17–19] and expansion velocities [6,9] v have become critical parameters. No time-resolved data for either have been published. Measurements of a related quantity, the critical density scale length $L = f(\int v\, dt)$ are available, but only averaged over the ionizing pulse [2] or for late delays (> 5 ps) [7]. By recording the spectral shifts incurred by a reflected picosecond probe pulse, we are able to measure time-resolved expansion velocities and ionization rates in critical density plasmas. The results are compared in detail with simulations combining one-dimensional (1D) hydrodynamics with numerical calculations of the spatial dependence of laser light absorption in arbitrary density gradient plasmas.

The experimental conditions are chosen to avoid many complicated laser plasma interactions such as resonance absorption and laser-induced parametric instabilities. The absorption could then be purely modeled by inverse bremsstrahlung and the frequency shifts could be purely attributed to plasma expansion and ionization. By contrast, for higher intensities and/or longer-scale-length plasmas ($I\lambda_\mu^2 kL > 3 \times 10^{18}$ W cm$^{-2}\mu$m^2, where I, k, and λ are the incident laser intensity, vacuum laser wave number, and wavelength, respectively), substantial hot-electron production from stimulated Raman scattering [22] at densities below quarter-critical density ($n_c/4$) is expected. The two plasmon decay instability [22] at $n_c/4$ is an additional source of underdense absorption for $I\lambda_\mu^2 kL/T_e > 5 \times 10^{13}$ W cm$^{-2}\mu$m^2 eV^{-1}, where T_e is the electron temperature. We note that the respective scattered light spectra from these two processes are at $\geq 2\lambda$ and $\frac{2}{3}\lambda$, and hence would *not* interfere with the interpretation of non-relativistic Doppler-shifted spectra. Small "red" shifts from stimulated Brillouin scattering [22], however, will compete [23] with "blue" Doppler shifts above a threshold of $I\lambda_\mu^2 kL/T_e = 3 \times 10^{13}$ W cm$^{-2}\mu$m^2 eV^{-1}. Hence all experiments reported here operated below $I\lambda_\mu^2 kL/T_e = 5 \times 10^{12}$ W cm$^{-2}\mu$m^2 eV^{-1} to avoid all parametric processes. In addition, profile steepening [24] by the laser ponderomotive force has been mitigated by staying well below the threshold [22] $I\lambda_\mu^2/T_e = 3 \times 10^{12}$ W cm$^{-2}\mu$m^2 eV^{-1} and by using s-polarized light.

In Sec. II, simple analytic results for frequency shifts in time-varying, exponential density profile plasmas are presented. Modeling of the plasma evolution is described in Sec. III. The experimental parameters, techniques and sample raw data are outlined in Sec. IV. Results and theoretical fits are presented and discussed in Sec. V. Conclusions and suggestions for future work are given in Sec. VI. In Appendix A, the density at which maximum absorption and reflection occurs for light incident on ultrashort-scale-length plasmas is calculated. In Appendix B, more analytic results for frequency shifts in expanding, ionizing, or recombining plasmas are tabulated and discussed for a variety of plasma geometries.

II. FREQUENCY SHIFTS

It was recognized 20 years ago that light passing through a media undergoing a time-varying refractive in-

dex will be frequency shifted [25]. Shifts were first observed for CO_2 laser pulses focused in air to create underdense breakdown plasmas [26], where the necessary refractive-index change was caused by the generation of free electrons. Recent, time-resolved femtosecond studies [27] in rapidly ionizing, underdense plasmas have demonstrated that the transmitted spectra can yield information on ionization rates and hence on ionization mechanisms. In addition, several proposals for producing relativistic shifts and pulse shortening using counter propagating laser pulses in ionizing gases have appeared [28–31].

We extend the technique here to the large density gradient plasmas common to laser–solid-target experiments. In addition to the phase modulation caused by ionization or recombination, hydrodynamic motion of such spatially inhomogeneous plasmas can also produce frequency shifts [6,9,32]. For the former, only electron-density variations are required; for the latter, space-charge-coupled ion and electron flows are in effect. In both cases, the imposed frequency shift can be divided into two contributions: a Doppler shift due to motion of the critical density surface where light reflection occurs, and an additional generally less important frequency shift during light passage through the time-varying subcritical-density portion [32].

To quantify these statements, we consider the frequency shift of a plane wave incident on an expanding (contracting) [6,32] or ionizing (recombining) [33,34] semi-infinite 1D plasma with a peak density n_0 greater than critical density. The plasma has a density gradient in the x direction with scale length L. We initially restrict ourselves to the WKB approximation only strictly valid for $kL > 1$, where k is the vacuum laser wave number. However, numerical calculations presented in Appendix A bridging the WKB limit and the Fresnel limit ($kL = 0$) suggest the following simple analysis can still be used to relate frequency shifts to plasma density profile evolution for kL as steep as 0.02. In addition we only consider the nonrelativistic limit leading to small frequency shifts ($\Delta\omega/\omega \ll 1$). Under these conditions, a plane wave incident at an angle θ has a well-defined turning point $n_{TP} = n_c\cos^2\theta$, where n_c is the critical density. The frequency shift is then given by [26,27,35]

$$\Delta\omega/\omega = -(2/c)\int_{n_e = n_{TP}(t)}^{n_e = 0} \frac{\partial n(x,t)}{\partial t} \frac{dx}{\cos\theta'} , \qquad (1)$$

where by Snell's law

$$\cos\theta' = [1 - (\sin\theta/n)^2]^{1/2} \qquad (2)$$

and where n is taken to be the usual real part of the refractive index

$$n = (1 - \omega_p^2/\omega^2)^{1/2} = (1 - n_e/n_c)^{1/2} \qquad (3)$$

and ω and ω_p are the laser and plasma frequency, respectively.

In Eq. (3), the plasma collisionality term ν/ω is omitted. It can be easily shown that the frequency shift contribution from changing collisionality in not unduly steep gradient plasmas ($kL \gg 0.1$) is at least a factor $2\nu^2/\omega^2$ smaller than the contribution from changing density (see

Appendix B). Since the maximum measured ν/ω at the maximum relevant density n_c is 0.1–0.3 for picosecond laser plasmas [1,2,7,8], the collisionality term can be safely ignored. Substituting Eqs. (3) and (2) into (1),

$$\frac{\Delta\omega}{\omega} = \frac{1}{c}\int_{n_e = n_{TP}(t)}^{n_e = 0} \frac{(1/n_c)[\partial n_e(x,t)/\partial t]dx}{[\cos^2\theta - n_e(x,t)/n_c]^{1/2}} . \qquad (4)$$

A. Shifts by hydrodynamic motion

We model the early evolution of picosecond laser plasmas with a self-similar exponential isothermal density profile [7], consistent with computer simulations presented in Sec. III. The self-similar density profile, shown in Fig. 1(a), is given by [22]

$$n_e = n_0\exp - (x/c_s t + 1) \quad \text{for } x > -c_s t , \qquad (5)$$

where n_0 is the solid-target density $L = c_s t$, $c_s = \sqrt{ZT_e/m_i}$ is the isothermal sound speed and m_i is the ion mass. From Eqs. (4) and (5), the frequency shift is [32]

$$\Delta\omega/\omega = 2(c_s/c)\{[\ln(n_0/n_{TP}) - 1] + 2(1 - \ln2)\}\cos\theta$$

$$= (2\cos\theta/c)[v_{TP} + 2(1 - \ln2)dL/dt] , \qquad (6)$$

where the turning point velocity is $v_{TP} = c_s[\ln(n_0/n_{TP}) - 1]$.

The first and second terms describe the motion of the turning point and the increase in plasma line density below n_{TP}, respectively. For $n_0/n_{TP} \approx 100$, a typical value for the experiments to the presented later, the second term contribution is $\approx 15\%$.

B. Shifts by ionization front motion

We consider a partially ionized plasma with initially an exponential density profile irradiated by an ionizing laser pulse of short enough duration that we may ignore hydrodynamic motion. For simplicity, we assume initially that (a) the ionization rate $S = d\ln Z/dt$ is constant in
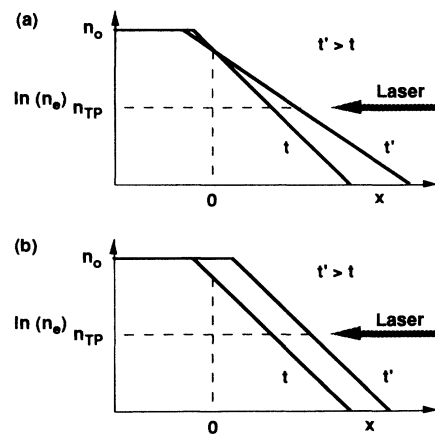

FIG. 1. (a) Self-similar density profile for isothermal expansion. (b) Ionization in isothermal density profile.

time, (b) the ionization rate is faster than the heating rate, thus maintaining local thermodynamic equilibrium, and (c) the plasma remains isothermal in space at any given time t to ensure a constant charge state Z at all x. Under those conditions, the electron density evolution is given by

$$\frac{dn_e(x,t)}{dt} = Sn_e(x,t) \ . \tag{7}$$

Hence the resultant density profile [Fig. 1(b)] is

$$n_e(x,t) = n_e(x,0)\exp(St) = n_0\exp-(x/L+1)\exp(St) \ . \tag{8}$$

The density profile given by Eq. (8) greatly simplifies the frequency shift calculation by having a constant scale length or, equivalently, separable time and space dependences. From Eqs. (8) and (4), the frequency shift is

$$\Delta\omega/\omega = 2(L/c)S\cos\theta = 2(L/c)\frac{d\ln Z}{dt}\cos\theta \ , \tag{9}$$

where $n_e(x,t) = n_i(x)Z(t)$ and n_i is the ion density.

By comparison with the first term in Eq. (6), the turning point velocity v_{TP} has been replaced by an ionization front velocity $L(d\ln Z/dt)$. Hence for sufficiently large L and/or ionization rates, the ionization front velocity should exceed the hydrodynamic velocity. For recombination, $d\ln Z/dt$ and $\Delta\omega/\omega$ are negative leading to a red shift. Analogous to the second term in Eq. (6), ionization in a plasma with a density-dependent scale-length yields an additional frequency shift term proportional to dL'/dt, where L' is the local scale length at the turning point density (see Appendix B). Similarly, for a nonequilibrium plasma in which the heating rate exceeds the ionization rate, profile steepening can occur and hence also yield an extra, in this case negative, time-dependent frequency shift term (see Appendix B).

III. COMPUTER MODELING

To simulate the experiments presented later, we use the laser fusion modeling program LASNEX [36]. LASNEX is run in only one dimension as the critical density surface moves $<5\%$ of the spot size ($\approx 100 \ \mu$m) in all cases modeled. The motivation for using LASNEX is to take advantage of the numerical physics options available in the code, such as time-dependent Lagrangian hydrodynamics, average ion atomic physics, Thomas-Fermi as well as nonequilibrium equations of state, flux-limited electron conduction and various types of radiation transport of which flux-limited diffusion was used here. The initial spatial mesh size at the target surface (density n_0) was set as small as 0.01 nm, which for $n_0/n_c \approx 100$ corresponds to a subsequent spatial resolution of 1 nm at critical density. In addition, a new subroutine was incorporated in LASNEX which calculates the absorption of short pulse-plane-wave electromagnetic radiation in a plasma. The package was designed to propagate light pulses of ≈ 100 fs or more duration, which corresponds to a minimum of ≈ 50 wave cycles in the visible. Since skin depths range from ≈ 10 to 100 nm, light traversal times are less than 1

fs, and hence density profile motion due to hydrodynamics and ionization can be ignored on this time scale. By Fourier transforming Maxwell's equations in space and time, and choosing the time steps between cycles in LASNEX sufficiently small such that the problem is effectively static, the above considerations lead to an approximation of Maxwell's equations in 1D known as the Helmholz equations. Our numerical algorithm for the solution of these equations reproduces the results of previous work [2,4,7,8]. Thus, during each LASNEX time step the subroutine solves the Helmholz equations for the incident wave in s and/or p polarization and then calculates the rate of Ohmic energy absorption $|J\cdot E| = \sigma_r|E|^2$, where σ_r is the real part of the conductivity and E is the complex electric field. The calculated energy absorption rate is then passed to LASNEX as a source. Absorption by other processes such as multiphoton ionization [37] and ionization dephasing [18] are estimated to contribute less than 1% absorption here and hence are ignored. In addition, the present experiments used only s polarization to suppress localized resonance absorption mechanisms [38].

The frequency-dependent conductivity which is needed in the wave equation is calculated using a generalized model of a dc calculation developed by Lee and More [39]. The generalization consists of accounting for the frequency dependence by interpolation between the dc conductivity of Lee and More and the high-frequency free-electron-gas conductivity. Lee and More accounted for solid-state effects by adjusting the calculated electron collision rate to be consistent with the electron mean free path in the material. Solid-state effects result in a falling off of the resistivity at high temperature which has been observed experimentally [1]. In addition, the conductivity is taken to be independent of intensity since the quiver energy of the electrons is always less than 20% of the electron thermal energy for the cases considered here.

The laser pulses are modeled as spatially uniform over the focal spot, but with a hyperbolic secant squared temporal profile which represents a good fit to autocorrelation traces. Figure 2 shows plasma parameters predicted by LASNEX calculations during irradiation, by a 583-nm, 1-ps full width at half maximum (FWHM), 1.5×10^{14}-W cm^{-2} pump pulse, of (a) a gold target and (b) a gold plasma performed 200 ps earlier by a 583-nm, 1-ps FWHM, 2×10^{13}-W cm^{-2} pulse. Both the performing pulse and pump pulse were incident at 10°. Figures 2(a) and 2(b) represent the state of the plasma at the peak of the pump pulse and show spatial profiles of the electron temperature T_e (in eV), the ionization state Z, and the plasma ion density ρ (in g cm^{-3}) and electron density n_e divided by the critical density $n_c = 3.28\times10^{21}$ cm^{-3}.

Figure 2(a) illustrates that the predicted early plasma profile is exponential and isothermal up to density $10n_c$. In Fig. 2(b), corresponding to a 200-ps delay after initial plasma production, the ion density profile has acquired a density-dependent scale length, but is still well approximated over any one scale length by an exponential. The electron density profile, however, has formed a plateau at critical density due to ionization by the pump pulse, as has been previously noted in other computational studies [17]. Since, during pump pulse irradiation, the electron

heating rates quickly surpass the electron collisional ionization rates at the relevant densities, critical density and below, it is essential to use non-thermodynamic equilibrium in LASNEX for electron temperatures as low as 20 eV to correctly evaluate time-dependent ionization states and hence critical density contour velocities. It should be mentioned that non-thermodynamic equilibrium also affects the plasma equation of state since the electron pressure is directly related to the electron number density.

Figure 2(b) also shows that the turning point density ($\approx 4n_c$) for a 2ω probe ($\lambda = 290$ nm) lies above the density plateau and hence is about 2-μm deeper into the plasma than the reflection point for a 1ω probe. In addition, the electron temperature at $\approx 4n_c$ is 1 eV, two orders of magnitude less than T_e at n_c. The combination of increased
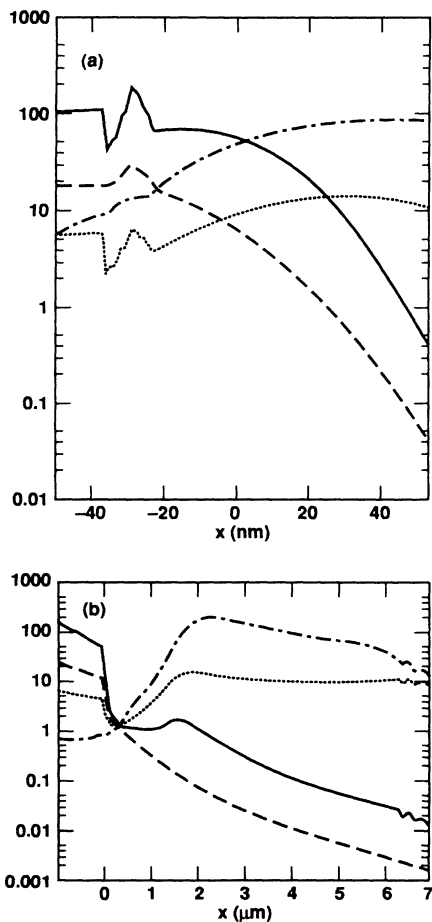
path length and decreased temperature should lead to much larger plasma absorption of 2ω radiation, an important experimental issue further discussed in Sec. V.

IV. EXPERIMENTAL SETUP AND RAW DATA

The experimental configuration is shown in Fig. 3. The laser consists of an amplified, synchronously pumped 3-mJ, 0.8–1-ps dye laser [40] operated at 580 or 583 nm and at a repetition rate of 2.5 Hz. The prepulse fluence on target was kept below 0.1 J cm^{-2} to avoid production of a long-scale-length plasma before arrival of the picosecond pulse. 10% of the laser energy, however, was contained in a 3-ps FWHM post pulse centered 7–8 ps after the main pulse. The laser beam was split into three to provide optically synchronized probe, pump and preforming plasma pulses with variable time delay between any two. The pump and preforming beams were focused by an $f/20$ lens to a 50–60-μm-dia spot at 5°–10° incidence. The s-polarized probe beam was focused by an $f/10$ lens to a 25-μm-diam spot at 30°–40° incidence and centered on the larger spot defined by the other two beams. The intensities of the probe, pump, and preforming plasma pulses were typically 2×10^{12}, 2×10^{14}, and 2×10^{13} W cm^{-2}, respectively. Experiments recording time-resolved spectral shifts on a single shot were also performed. In that case, the probe beam consisted of optically synchronized 532-nm, 1-μJ, 70-ps FWHM pulses.

The targets consisted of 3-in. polished silicon wafers (0.3-nm rms surface roughness) overcoated with 500 nm of gold or carbon. The targets were mounted on remotely driven translation and rotation stages so the laser could fire on a fresh target surface on each shot. The target manipulator and focusing optics were mounted in a vacuum chamber operating at a base pressure of 3×10^{-5} Torr. The specular reflection of the probe pulse was imaged onto the slits of a 0.34-m grating spectrometer attached to an optical multichannel analyzer (0.57 Å per pixel) and oscilloscope. Spectra were averaged over 30–40 shots and the shift of the spectral peak was recorded at each intensity or temporal setting. Shot-to-shot spectral jitter was less than 0.3 Å. For the long pulse probe, the spectrometer was coupled to a fast (3-ps resolution) streak camera.

The spectra of a single pulse reflecting from a gold target at 40° incidence is shown in Fig. 4 for increasing pulse
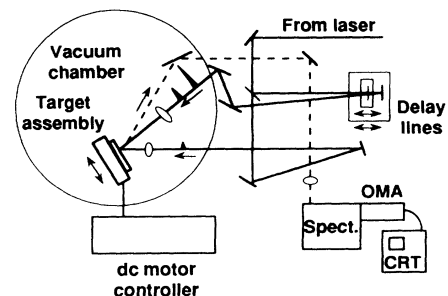

FIG. 2. 1D hydrodynamic simulation of plasma parameters present at peak of 1-ps, 1.5×10^{14}-W cm^{-2} pump pulse during irradiation of (a) solid gold target and (b) gold plasma created 200 ps earlier by a 1-ps, 2×10^{13}-W cm^{-2} preforming plasma pulse. Both pulses s polarized and incident from positive x at 10° to the target normal. Curves are for normalized electron density n_e/n_c (solid line), ion density in g cm^{-3} (dashed line), electron temperature T_e in eV (dot-dashed line), and average charge state Z (dotted line). Initial target surface is at $x=0$.
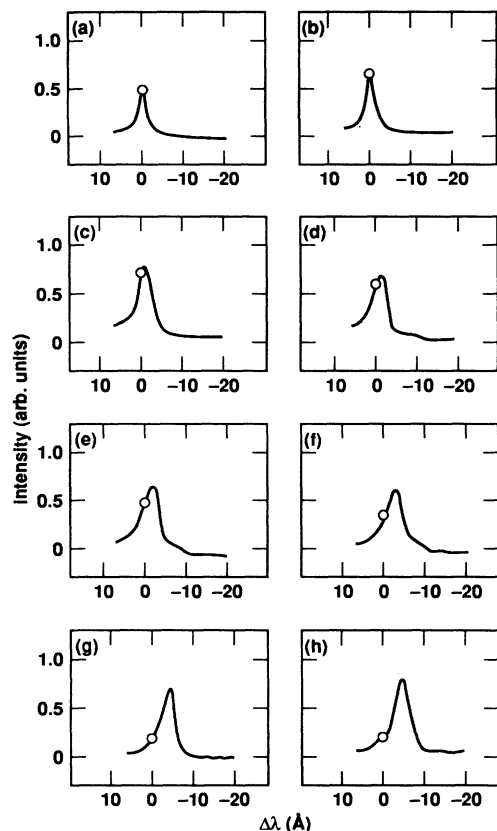

FIG. 3. Experimental configuration.

FIG. 4. Reflected s-polarized pulse spectra for various peak irradiances on gold target: (a) $I = 4.4 \times 10^{11}$ W cm^{-2}, (b) 1.2×10^{12} W cm^{-2}, (c) 6.2×10^{12} W cm^{-2}, (d) 2.2×10^{13} W cm^{-2}, (e) 6.8×10^{13} W cm^{-2}, (f) 1.6×10^{14} W cm^{-2}, (g) 2.3×10^{14} W cm^{-2}, (h) 4×10^{14} W cm^{-2}. Pulse incident at 40°.

FIG. 5. Spectrum of 3×10^{14}-W cm^{-2} pump pulse reflecting at 40° from gold plasma formed 200 ps earlier by 2×10^{13}-W cm^{-2} pulse. Unshifted component is due to post pulse.

strumental resolution offered by the streak camera, as dictated by the uncertainty limit $\Delta \nu \Delta \tau \approx 0.5$. A prompt 2-Å blue shift is observed, which decreases on a 10-ps time scale and is obscured after 15 ps by a rapid decrease in plasma specular reflectivity. At lower pump intensities, the peak shift decreases, consistent with Fig. 4, and the specular reflectivity persists longer.

The spectral-shift–to–width ratios after deconvolution of the finite laser bandwidth are high, typically 3 at the higher irradiances. Hence we surmise that the contributions to spectral broadening such as temporal averaging $(\partial^2 n / \partial t^2)$ over the pulse duration, spatial averaging over the focal spot and over steep plasma density profiles, are small and can be ignored in all further analyses. Thus only the frequency shifts of the peaks in the reflected spectra will be plotted hereafter and compared to computer simulations.

irradiance I. The unshifted spectra [Fig. 4(a)] consisted of a 2.5-Å FWHM peak superimposed on a weaker 10-Å-wide component centered slightly to longer wavelengths. The spectra were in all cases shifted to higher frequency. The data closely parallel those of Milchberg and Freeman [6], where the shift which is proportional to $\partial n / \partial t$ [see Eq. (1)] increases as $\sqrt{I}$.

The spectrum of a 3×10^{14}-W cm^{-2} pulse reflected at 40° from a gold target irradiated 200 ps earlier by a 2×10^{13}-W cm^{-2} pulse is shown in Fig. 5. By comparison with Fig. 4(g) or 4(h), the shift has increased fivefold. The large increase is attributed to ionization front motion in a preformed long density scale-length plasma as described by Eq. (9). From streaked spectra, the unshifted component in Fig. 5 was identified as the undesirable low-intensity post pulse.

Time-resolved spectra using the long pulse probe are shown in Fig. 6. The incidence angles of the pump and probe beams were 5° and 40°, respectively, the pump intensity was 1×10^{14} W cm^{-2}, and there was no preforming plasma pulse. The absolute timing has been calibrated by recording in zeroth order the relative arrival of specularly reflected 532-nm probe light and diffusely reflected 583-nm pump light. Note that the spectral resolution has been purposely set at 2 Å to retain the 3-ps in-
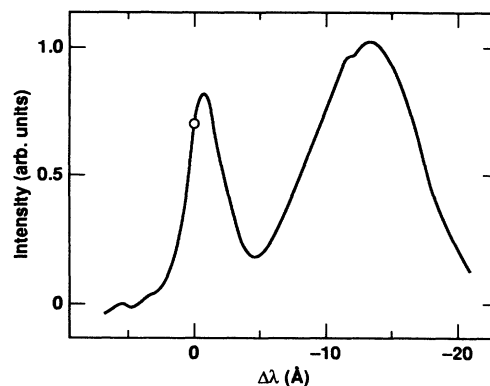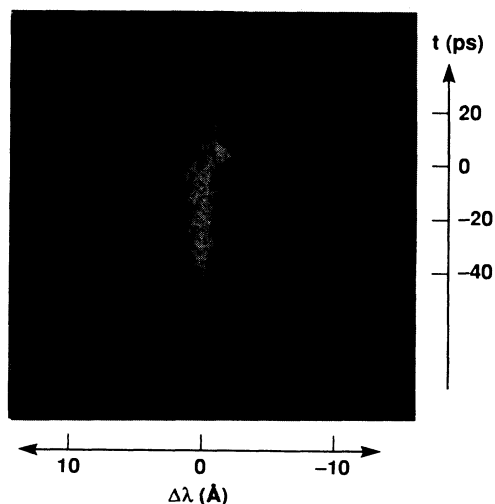

FIG. 6. Streaked spectrum of s-polarized 532-nm, 70-ps probe pulse reflecting at 40° from gold target irradiated at $t = 0$ by 583-nm, 1-ps, 1.5×10^{14}-W cm^{-2} pulse.

V. RESULTS AND ANALYSIS

In Fig. 7, the spectral peak shifts measured from the single-pulse data on Fig. 4 are plotted versus peak laser irradiance. Moreover, since the modeling predicts exponential profiles throughout the pulse, Eq. (6) has been used on Fig. 7 to translate frequency shifts into expansion velocities at the turning point density ($n_{TP} = 1.9 \times 10^{21}$ cm^{-3}). The solid curve is the calculated shift from the computed time-dependent profiles, convolved over the finite pulse duration and including both turning-point density motion and scale-length evolution below n_{TP}. We note that the data and shifts extracted from the simulations by assuming reflection at the classical turning point density, $n_c \cos^2\theta$, are in surprisingly good agreement given the calculated ultrashort scale lengths present ($L = 2-14$ nm or $kL = 0.022-0.15$). Specifically, in such steep plasma gradients, Eq. (6) should be invalid, the majority of the absorption will occur well above n_{TP} [2,4] and significant reflection will occur over a large range of densities at and above n_{TP}. However, poorer fits are obtained by simply postulating a higher turning-point density which travels at a lower velocity.

The agreement in Fig. 7 is less surprising by noting that we are plotting the shift of the spectral *peak*, which after deconvolution of the initial laser spectra profile, is a measure of the velocity of the density contour yielding *maximum* reflectivity. This highlights an important distinction between ultrashort scale length plasma absorption [2,4] and reflection. The absorption, predominantly collisional, varies as $n_e n_i I(x)$ but the plasma reflectivity above n_{TP} is only weakly dependent on density and so just varies with $I(x)$, the laser intensity. For s-polarized light, the well-known solution [22] for $I(x)$ yields a standing wave below n_{TP} and an exponentially decaying wave above n_{TP}. Hence, as shown on Fig. 12 in Appendix A, while the calculated density for maximum absorption varies approximately [4] as $n_{TP}/(kL)^{4/3}$ for $kL < 1$, the density at which the maximum reflection occurs remains close to the usual turning point density n_{TP}, where $I(x)$ is still unattenuated, even for kL as short as 0.02. Thus, for $I > 3 \times 10^{13}$ W cm^{-2}, we conclude that the shifts of the peaks in the reflected spectra shown in Fig. 4 and plotted in Fig. 7 are indicative of the usual

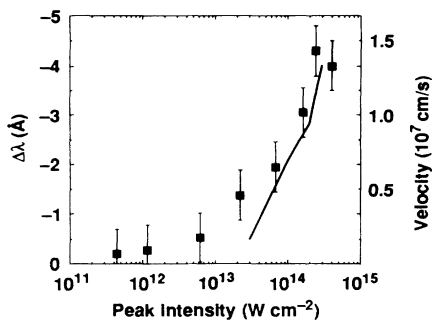turning-point density velocity. For $I < 3 \times 10^{13}$ W cm^{-2}, for which kL is less than 0.02 at the peak of the pulse, calculations predict that at least 50% of the laser pulse passes through the plasma reflects from the unablated solid target and suffers no frequency shift. Hence the small spectral shifts observed below $I = 3 \times 10^{13}$ W cm^{-2} are more complicated reflectivity averages over moving plasma and undisturbed solid.

In Fig. 8(a), the spectral shifts and inferred velocities at n_{TP} experienced by a pump pulse interacting with preformed gold (e.g., Fig. 5) and carbon plasmas are plotted as a function of delay Δt between preforming plasma pulse ($I = 2 \times 10^{13}$ W cm$^{-2}, \theta = 10°$) and pump pulse ($I = 3 \times 10^{14}$ W cm$^{-2}, \theta = 40°$). The solid curve represents theoretical predictions for several delays in gold plasmas, each one weighted over the pump pulse temporal profile. The experimental and calculated shifts are in good agreement, decreasing slightly before rising sharply after $\Delta t = 50$ ps. The results indicate a transition from purely hydrodynamic motion to dominance by ionization front motion as Δt and hence L increases. As an example of the importance of ionization, consider the effective measured turning-point velocity of 7×10^7 cm s^{-1} at $\Delta t = 500$
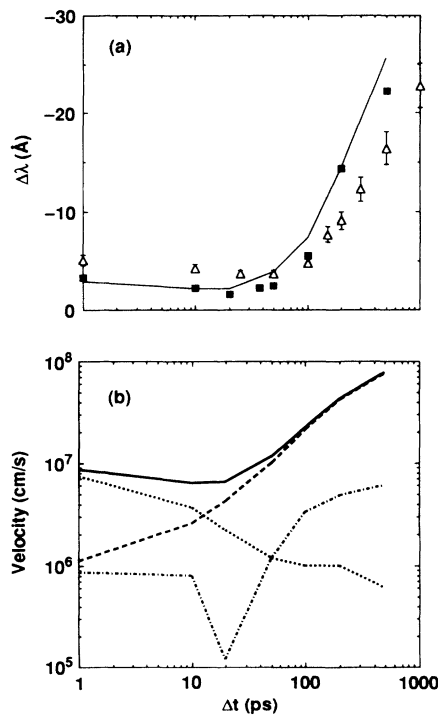

FIG. 8. (a) Wavelength shifts incurred by pump pulse versus delay after initial plasma production for gold (solid squares) and carbon (open triangles) targets. Preforming plasma pulse irradiance is 2×10^{13} W cm^{-2} at 10° incidence and pump pulse irradiance is 3×10^{14} W cm^{-2} at 40° incidence. Solid curve is theoretical calculation for gold. A-10-Å shift translates to a Doppler velocity of 3.3×10^7 cm/s. (b) Calculated shifts (velocities) versus delay. Solid line is total, dotted line is contribution from hydrodynamic motion, dashed line is contribution from ionization, dash-dotted line is contribution from changing scale length.

FIG. 7. Wavelength shifts from data of Fig. 4 vs peak laser irradiance. Solid curve is theoretical fit.

ps. If such a velocity were solely hydrodynamic in origin, Eq. (6) predicts ZT_e would be 60 keV, clearly much too high for the present incident laser intensities and sub- to few keV spectra recorded [11]. Moreover, ascribing the shift solely to ionization for the calculated scale length of 1.5 μm at $\Delta t = 500$ ps leads to $d \ln Z/dt = 0.5$ ps^{-1}, a reasonable 60% increase in the value of Z during the peak of the picosecond pump pulse. For the other time delays for which ionization front motion dominates, 50, 100, and 200 ps, the ionization rates $d \ln Z/dt$ during the pulse peak are 0.3, 0.4, and 0.5 ps^{-1}, respectively. By contrast, for a small delay such as 1 ps during which L has only reached 20 nm, ignoring the hydrodynamic contribution to the shift leads to a predicted $d \ln Z/dt = 3.8$ ps^{-1}, an unrealistic 45-fold increase in the charge state during the peak of the pulse. Conversely, ignoring an ionization contribution at $\Delta t = 1$ ps yields $ZT_e = 600$ eV, in fair agreement with simulations ($Z = 15$, $T_e = 60$). For carbon, the smaller shifts recorded at late time delays are ascribed to fewer charge states available in ionizing carbon.

More detailed results for the various calculated contributions to the shifts in gold plasmas are shown in Fig. 8(b) as a function of time delay. The various shifts have been translated into effective Doppler velocities v by $\Delta\omega/\omega = 2(v/c)\cos\theta$. The maximum calculated shift imparted by changing collisionality translates to $< 1 \times 10^4$ cm s^{-1} and hence is ignored. As surmised above, hydrodynamic motion contributes 90% of the shift at the earliest delay (1 ps), while ionization front motion contributes 99% of the shift at the largest delay investigated, 500 ps. Equal shift contributions are predicted to occur between 10- and 20-ps delay, when L reaches 100 nm. We note that the contribution from changing scale-length is 13% at $\Delta t = 1$ ps, consistent with the analytic solution for the isothermal expansion model shift [Eq. (6)]. As expected, the absolute value of the shift contribution from dL/dt first decreases with delay as the sound speed $c_s = dL/dt$ decreases, but then rises sharply after $\Delta t = 20$ ps. The reason for the subsequent increase is linked to the predicted departure from a purely exponential profile for $\Delta t > 10$ ps, for which times the unperturbed profile is approximately given by

$$n_e(x) = n_0 \exp - [2x \ln(n_0/n_c)/L]^{1/2} ,$$

where L remains as the critical density scale length, but the general scale length $L^* = [2xL/\ln(n_0/n_c)]^{1/2}$ is density dependent, increasing with increasing x (decreasing density). Since the turning point during ionization by the pump beam moves to larger x where L^* is longer, additional "blue" shift terms appear due to dL/dt (see Table I in Appendix B).

The results presented in Figs. 7 and 8 were time resolved by interrogating with a probe pulse, the frequency shifts before, during and after pump pulse irradiation. The evolution of shifts in a gold plasma irradiated at 10° incidence by a 1-ps, 1.5×10^{14}-W cm^{-2}, 580-nm pump pulse, with and without a 2×10^{13}-W cm^{-2} preforming plasma pulse arriving 200 ps earlier, are shown in Fig. 9 on an expanded scale. The probe pulse intensity, 2×10^{12}
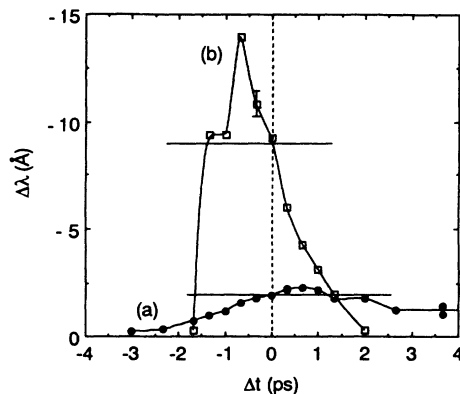
FIG. 9. Variable delay probe pulse shifts during pump pulse irradiation: (a) without and (b) with preforming plasma pulse on gold target. Probe pulse irradiance is 3×10^{11} W cm^{-2} at 30° incidence, preforming plasma pulse irradiance is 2×10^{13} W cm^{-2} at 10° incidence, pump pulse irradiance is 1.5×10^{14} W cm^{-2} at 10° incidence, and delay between the latter two pulses is 200 ps. Horizontal lines are pump pulse shifts and 0 delay corresponds to simultaneous arrival of pump and probe pulses.

W cm^{-2}, was checked to be noninvasive and the probe incidence angle was 30° for a turning point density $n_{TP} = 2.5 \times 10^{21}$ cm^{-3}. The two sets of data shown in Fig. 9 were taken under identical conditions except for intentional misalignment of the preforming plasma beam for curve a. Hence the temporal shift between the peaks in curves a and b is reliable even if absolute timing were not known. Absolute timing to within 0.3 ps was found as follows. After applying a small (10%) correction for the noncollinear geometry, the frequency shifts incurred by pump and probe pulses arriving simultaneously at the target (delay $\Delta t = 0$ ps) should be identical. Since the measured pump pulse shifts, denoted as horizontal lines on Fig. 9, are slightly less than the peak probe pulse shifts, two possible locations in time for $\Delta t = 0$ ps exist on curves a and b, one on the rising edge and one on the falling edge. However, since the peaks in curves a and b are displaced in time, only the rising edge location on curve a and the falling edge location on curve b match up and hence define $t = 0$ ps. Hence the peak ionization shift and peak Doppler shift occur 0.5–0.8 ps *before* and *after* the peak of the pump laser pulse, respectively.

In Fig. 10(a), time-resolved data without a preforming plasma pulse, similar to curve a on Fig. 9, is plotted over a longer time scale. The data are qualitatively similar to those of Fig. 6, but offer three times better temporal resolution. The frequency shift rise time, 4 ps, is slow and lags with respect to the laser pulse rise time, 1 ps. This is attributed to a predominantly hydrodynamic Doppler shift which increases cumulatively with absorbed laser energy fluence [6]. At $t = 0$ ps, the small (25%) variation in the shift over a 1-ps interval can quantitatively explain the large shift-to-broadening ratio observed in the single beam experiment (Fig. 4). The effect of the undesirable pump post pulse manifests itself as a second peak centered at 8-ps time delay. This second peak is attributed to additional ionization ($d \ln Z/dt = 0.1$ ps^{-1}) rather
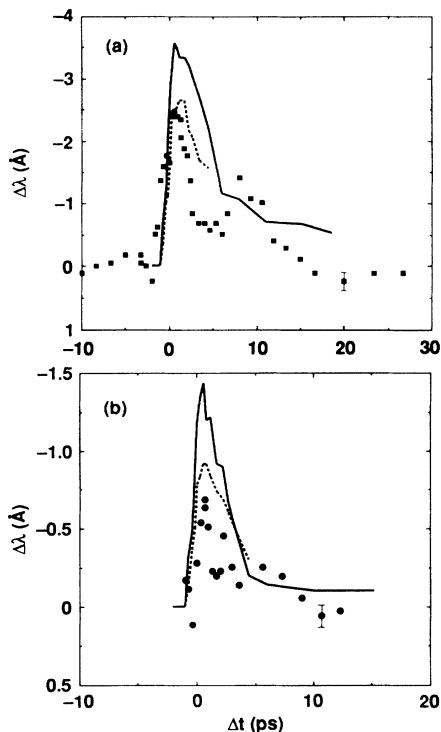
FIG. 10. Variable delay probe pulse shifts during pump pulse irradiation, without preforming plasma pulse, using (a) 580- and (b) 290-nm probe pulses. Pump pulse irradiance is 1.5×10^{14} W cm^{-2} at $10°$ incidence. A 1-Å shift translates to Doppler velocities of 3×10^6 cm/s and 6×10^6 cm/s for (a) and (b), respectively. Solid curve and dashed curve are simulation results at 1.5 and 0.75×10^{14} W cm^{-2}, respectively.

and weighted over the finite probe pulse duration are shown as solid curves on Figs. 10(a) and 10(b). The theoretical results reproduce the early temporal behavior of the measured shifts, peaking at $t = 1$ ps and then initially decaying on a 3–5 ps time scale. The initial shift decay is caused by both the electron temperature T_e decreasing from a peak of 70 to 25 eV and the charge state Z dropping from 15 to 11 and from 16 to 7 at the 580- and 290-nm turning-point densities, respectively. However, the absolute magnitude of the calculated shifts are 30–50 % higher than observed and remain nonzero at late times (15–30 ps). The calculations also predict a smaller 17% reduction in the relative $(\Delta\lambda/\lambda)$ peak shifts between Figs. 10(a) and 10(b). Better fits shown as dotted curves on Figs. 10(a) and 10(b) are obtained by assuming a 50% lower pump pulse intensity of 7.5×10^{13} W cm^{-2}, corresponding to the lower error limit on the experimental intensity.

In Fig. 11(a), time-resolved data with a preforming plasma pulse, similar to curve b in Fig. 9, is plotted over a longer time scale. By contrast with Fig. 10(a), a much larger and more transient shift is obtained with a 2-ps rise time and 1-ps decay time. The results of Fig. 11(a) are consistent with ionization front motion, where the ionization rate first increases with absorbed laser intensity, then decreases rapidly with increasing charge state (ionization potential), and finally disappears altogether as ionization itself ceases with the onset of plasma cooling. Careful measurements at late delays show no observable red

than hydrodynamic acceleration, because the calculated long-prevailing scale length at $t = 8$ ps (270 nm vs 20 nm at $t = 1$ ps) favors ionization-induced shifts, as previously discussed in reference to Fig. 8(b). At later delays, the frequency shifts and hence sound speeds become undetectable within 20–30 ps, consistent with earlier time-resolved scale-length measurements [7] and suggestive of rapid cooling of electrons by thermal conduction and/or recombination. It should also be noted that the frequency shifts after 10 ps could be a combination of red recombination shifts and blue hydrodynamic shifts.

In Fig. 10(b), the probe was switched to a 10^{11}-W cm^{-2} frequency-doubled ($\lambda = 290$ nm) pulse which reflects at a higher density, $4n_{TP} = 10^{22}$ cm^{-3}. Since the difference in pump and probe wavelength precluded finding $\Delta t = 0$ ps as before (Fig. 9), absolute timing was estimated to ± 1-ps accuracy by applying a calculated 20-ps correction for the group velocity delay between 580- and 290-nm light in the relevant optics before the target. The features of Figs. 10(a) and (b) are similar, including evidence of the post pulse. The measured 40% reduction in relative shift $\Delta\lambda/\lambda$ for the shorter wavelength probe is in fair agreement with the 31% reduction predicted by the isothermal expansion model [Eq. (6)], where the exact value of n_0/n_c is not critical and taken to be 100.

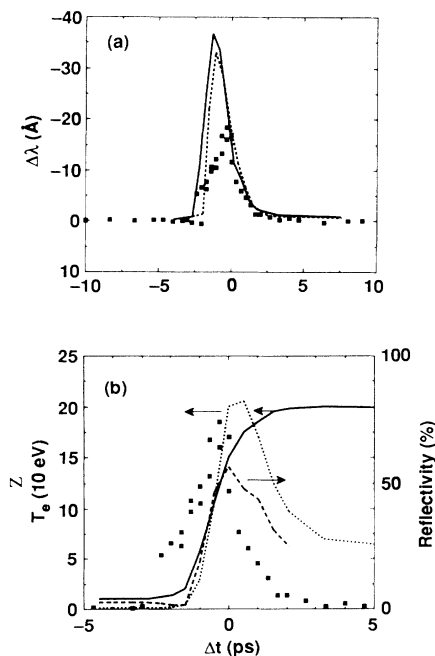The computational predictions ignoring the post pulse

FIG. 11. (a) Variable delay probe pulse shifts during pump pulse irradiation, with preforming plasma pulse. Parameters identical to Fig. 9(b). Solid and dashed curves are computational results at 1.5 and 0.75×10^{14} W cm^{-2}, respectively. (b) Expanded plot, superimposing on data calculated evolution of plasma reflectivity (dashed line), temperature (dotted line), and charge state (solid line) at turning-point density.

recombination shifts which again may be masked by small blue Doppler shifts. The area under Fig. 11(a) yields a total displacement $L \Delta \ln Z = 0.7$ μm, which for a predicted scale length $L = 0.6$ μm equates to a threefold jump in Z.

Attempts to repeat these time-resolved shift measurements using a frequency-doubled probe pulse failed. No shifts were observed, in contradiction with a minimum peak shift of 1.2 Å predicted both by simulations and by extrapolating from the measured 580-nm probe shifts. It is likely that the sampled reflected uv probe light was predominantly unfocused radiation which did not interact with the plasma, suffering no absorption nor frequency modulation. Such a view is supported by noting that the calculated plasma optical depth τ ($\propto 1/\lambda^2$ for a purely exponential isothermal profile) is ≥ 7, while the measured ratio of the reflected probe signal with and without the plasma yields $\tau \leq 4$.

Computational results for the 580-nm probe, convolved with the finite probe pulse duration and with the time-dependent plasma reflectivity, are superimposed as curves on Fig. 11(a). The solid and dashed curves correspond to pump intensities of 1.5 and 0.75×10^{14} W cm^{-2}, respectively. The modeling reproduces the negative delay for the peak shift and agrees with the data at positive delays. However, the simulations predict up to 250% larger shifts during the leading edge of the pump pulse and hence a much greater time-integrated jump in charge state Z (15-fold versus 3-fold experimentally). Changing the assumed pulse profile over the region of interest ($-2.5 < \Delta t < 2.5$ ps) does not alter the area under the theoretical curve and hence does not remove the discrepancy. One solution is to postulate the presence of a long (> 10 ps) low-intensity prepulse which would slowly preionize the plasma such that the resultant shifts before $\Delta t = -2.5$ ps would be below our 0.2-Å detection threshold, yet the plasma charge state would have reached $Z = 5$ by $\Delta t = -2.5$ ps. However, the resultant long-scale-length plasmas caused by such prepulses [11] incident on solid targets, before arrival of the main picosecond pulse, has not been observed here and in other related experiments [7,41] using the same laser. We suggest spatially dependent reflectivity is at least part of the reason for the large difference between calculations and data at early delays ($\Delta t < -0.5$ ps) by examining the calculated evolution in plasma reflectivity, temperature, and charge state at the turning point density. Figure 11(b) shows that by virtue of the predicted plasma conditions immediately before pump pulse irradiation, that is, low charge state $Z = 1$ and long scale length $L = 0.5$ μm, the charge state can increase by a factor of 5 by $\Delta t = -1$ ps in the pump pulse profile while the plasma remains cold (< 20 eV) and hence highly collisional and absorbing ($> 90\%$). It is then likely that the measured spectra between $\Delta t = -2.5$ and -1 ps have been compromised just as in the uv probe experiment by the spatial wings of the 580-nm probe light which reflect from outlying, shorter scale length, hence more reflective plasma regions which undergo less ionization and hence impart smaller frequency shifts. We note that this phenomenon cannot explain the discrepancies between the full pump intensity

simulation and data for the time-resolved shifts without preformed plasmas (Fig. 10) as the specular reflectivity in such steep gradient plasmas begins and remains high, $> 50\%$ for a 580-nm probe for $\Delta t < 5$ ps, as shown on Fig. 6.

The predictions shown on Fig. 11(b) illustrate that, after the peak of the pump pulse, the electron temperature immediately begins to drop while the charge state continues to rise for a few picoseconds. Such behavior is indicative of a nonequilibrium plasma in which the ionization rates are slower than the heating and cooling rates. Hence, by using picosecond pulses, we are able to both leave a high-density (3×10^{21} cm^{-3}) plasma in a state of nonequilibrium and to noninvasively probe the dynamics of the subsequent equilibration process.

VI. SUMMARY

The evolution of critical density profiles in $< 10^{14}$-W cm^{-2} picosecond laser plasmas have been inferred from the spectral shifts imposed on reflected picosecond laser pulses. Peak spectral shifts of $\Delta\lambda/\lambda = -0.004$ have been recorded, corresponding to critical density velocities approaching 10^8 cm/s. Using simple analytic results, sound speeds and ionization rates are extracted from the measured spectral shifts for normalized density scale lengths kL as short as 0.03. In addition, the predicted dominance of hydrodynamic motion for short-scale-length plasmas and ionization front motion for long-scale-length plasmas have been observed and shown to agree with 1D computer simulations. The generally good fits between experiments and simulations confirm that parametric absorption and frequency shift mechanisms are, as expected, negligible under our conditions $I\lambda_\mu^2 kL/T_e < 5 \times 10^{12}$ W cm^{-2}μm^2eV^{-1}. The present method of inferring plasma dynamics from spectral shifts of reflected laser pulses should be applicable for all laser-plasma parameter space below $I\lambda_\mu^2 kL/T_e = 3 \times 10^{13}$ W cm^{-2}μm^2eV^{-1}. The simulations also indicate that the self-similar isothermal exponential density profile model is a good approximation up to 100-nm scale lengths. The time-resolved experimental results show more sensitivity to modeling and show only qualitative agreement between data and simulations. The poorer fits are attributed to contrast problems in measuring time- and space-dependent reflectivities and to uncertainties in laser irradiance. Nevertheless, the observed large qualitative differences in the amplitude and time dependence of the reflected spectral shifts with and without a preformed plasma (see Fig. 9) are reproduced by the computer simulations. Indeed, such characteristic temporal dependence in the reflected spectral shifts could be used as a sensitive measure of the degree of plasma preexpansion by laser prepulses and/or by the main pulse leading edge during high-intensity ultrashort-pulse laser-solid interaction experiments. The amount of pre-expansion in turn will be crucial in determining and in correctly modeling the mechanisms and degree of absorption of the main pulse.

Further experiments using several probe wavelengths spanning the infrared to far ultraviolet could map the

plasma velocity profile over a larger density range of 30 for a better test of hydrodynamic and ionization front expansion models. The shifts incurred during p-polarized pump irradiation might yield information on resonance absorption mechanisms where swelling of the laser field at critical density could lead to such high-intensity processes as multiphoton ionization. For a combination of short scale lengths and high intensity, profile steepening by the ponderomotive force at critical density [22] should reduce [42] the magnitude of blue expansion shifts and should eventually yield net red shifts due to predicted laser hole boring [43] above $I\lambda_\mu^2 = 10^{18}$ W cm$^{-2}\mu$m^2. Frequency shift measurements on laser plasmas with 10–100-fs pulses are a natural extension, but may prove more difficult due to the intrinsic larger laser bandwidth. In addition, the slower ionization rates and lower collisional rates effective in the interesting higher temperature plasma regime [3,20] accessible with intense shorter laser pulses will yield smaller spectral shifts. Both concerns might be alleviated by using a shorter wavelength probe which reflects at a higher density where collisional ionization rates are expected to be higher.

ACKNOWLEDGMENTS

APPENDIX A

To relate Doppler-shift measurements to plasma profile evolution calculations, the spatial dependence of the reflection must be known since each density contour will in general move at a different velocity [see Fig. 1(a) for example]. In the limit of long plasma density scale lengths $kL > 1$, reflection is localized at the turning point density $n_{TP} = n_c \cos^2\theta$ and hence only the velocity at n_{TP} matters. However, as the scale-length decreases below the optical skin depth ($kL < 1$), an electromagnetic wave incident on such a profile will penetrate above n_{TP} and hence sample a larger range of densities.

We first estimate the degree of reflection at each density by calculating the electric-field profile by numerically solving the Helmholz wave equations [8] for an exponential density profile of arbitrary scale length. Neglecting multiple reflections, the relative reflectivity at each point is then estimated by multiplying the square of the local-field amplitude by the local Fresnel reflectivity [44] at each density point. Second, we calculate, using Eq (6), the unique velocity and hence frequency shift which is imparted by each density contour. The reflected spectrum is then the distribution of frequency shifts from all densities, each of which is weighted by the reflectivity from that density. Hence the experimental observable,
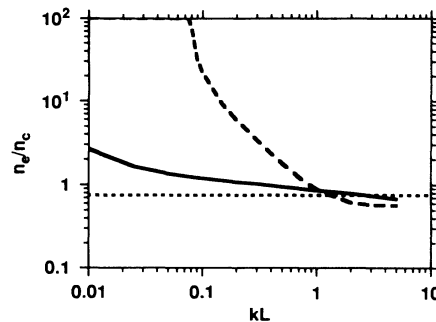

FIG. 12. Numerical results showing electron density at which maximum absorption (dashed line) and reflection (solid line) occurs versus plasma density scale length. Isothermal, exponential profile is used with normalized critical density collisionality $v/\omega = 0.3$, s-polarized light, and 30° incidence. Classical turning-point density n_{TP} is shown as dotted line.

the frequency shift of the peak in the spectrally resolved reflectivity, also occurs at the density for maximum reflectivity. The dependence of the density for maximum reflectivity on scale length is shown in Fig. 12 for s-polarized light, a collision frequency $v/\omega = 0.3(n_e/n_c)$ and 30° incidence. We also plot the density for peak absorption which is directly calculated from the Helmholz equations [2,4,7]. While the maximum absorption point is strongly dependent on scale length, varying as $(kL)^{-4/3}$, the density for maximum reflectivity remains within a factor of 2 of the classical turning point density for kL as short as 0.03, corresponding to $L = 3$ nm for 580-nm light. Hence, for $kL > 0.03$, we may still use Eq. (6) to relate the velocity of the turning point density to the measured experimental quantity, the shift of the peak in the spectrally resolved reflectivity.

APPENDIX B

In Table I, analytical results for spectral shifts incurred in plasmas with various initial and evolving density profiles are presented. For clarity, each of the three spectral shift mechanisms considered here, hydrodynamic motion, ionization, and changing collisionality, is isolated in turn. The initial target density is n_0 and the collisionality at critical density v_c/ω is β. For transverse probing, the plasma diameter d is introduced as an additional parameter and refraction is ignored. It should be noted that "normal" probing by reflection from the turning-point density transmutes into transverse probing as in plasma interferometry when $2L\tan\theta > d$. Profile steepening caused by, for example, density-dependent ionization rates or the laser ponderomotive force, is simulated using $L' = L - c_L t$ above a lower density n_L. For the two color cases, λ_1 designates the pump pulse and λ_2 the probe pulse; the critical density n_c and the turning point density n_{TP} are defined with respect to λ_1.

It is instructive to consider the relative magnitudes of shifts in the underdense region ($n_e < n_c$). For initially ex-

TABLE I. Analytic results for frequency shifts for various classes of evolving plasma density profiles, probe geometries, and wavelengths. H denotes hydrodynamic, I ionizing, C collisionality changing, E exponential profile, FT flat-top profile, L linear profile, CP computed profile, S steepened profile, F foil target, T transverse probing, and λ_2 probe wavelength, if different from pump wavelength λ_1.

Model	Density profile	Conditions	Shift ($\Delta\omega/\omega$)
H,E	$n_e = n_0\exp-(x/c_s t + 1)$	$\nu/\omega = \beta(n_e/n_c), \beta^2 \ll 1$	$2(c_s/c)\{[\ln(n_0/n_{TP})-1]+2[1-\ln2]$ $-\frac{8}{15}\beta^2\cos^4\theta\}\cos\theta$
$H,$FT$,F$	$n_e = n_c L_c/c_s t, |x| < c_s t/2$ $n_e = 0, |x| > c_s t/2$	$n_e < n_c, \theta = 0°$	$(-c_s/c)\{(1-L_c/2c_s t)/(1-L_c/c_s t)^{1/2}-1\}$
H,E,F	$n_e = (n_c L_c/2c_s t)\exp-x/c_s t$	$n_e < n_c, \theta = 0°$	$(-2c_s/c)\{A-2\ln(1+A)+2\ln2-1\}$, $A = (1-L_c/2c_s t)^{1/2}$
H,E,T	$n_e = n_0\exp-(x/c_s t + 1)$	$n_e \ll n_c, \theta = 90°$	$(c_s/2c)\{(d/L)[\ln(n_0/n_e)-1]$ $\times(n_e/n_c)/(1-n_e/n_c)^{1/2}\}$
I,E	$n_e = n_0\exp-(x/L)\exp St$	$S = d\ln Z/dt$	$(2L/c)(d\ln Z/dt)\cos\theta$
I,E,λ_2	$n_e = n_0\exp-(x/L)\exp St$ $n_e = n_0\exp-(x/L)$	$n_e < n_c, \lambda_2 < \lambda_1$ $n_e > n_c$	$(2L/c)\{1-[1-(\lambda_2/\lambda_1)^2]^{1/2}\}(d\ln Z/dt)\cos\theta$
I,E,S	$n_e = n_L\exp(x/[L-c_L t])$ $n_e = n_L\exp(x/L)$	$n_e > n_L$ $n_e < n_L$	$(2c_L/c)\{\ln[(1+B)/(1-B)]-2B\}\cos\theta$, $B = (1-n_L/n_{TP})^{1/2}$
I,E,S,λ_2	$n_e = n_L\exp[x/(L-c_L t)]$ $n_e = n_L\exp(x/L)$	$\lambda_2 = \lambda_1/2, n_{TP} > n_e > n_L$ $n_e < n_L, n_e > n_{TP} \gg n_L$	$(2c_L/c)\{0.134\ln(n_{TP}/n_L)$ $-2(0.134-0.101\ln2)\}\cos\theta$
$I,$FT$,F$	$n_e = (n_c L_c/L)\exp St, |x| < L/2$ $n_e = 0, |x| > L/2$	$n_e < n_c, \theta = 0°$	$(L/c)(d\ln Z/dt)(n_e/n_c)/(1-n_e/n_c)^{1/2}$
I,E,F	$n_e = n_0\exp-(x/L)\exp St$	$n_e < n_c, \theta = 0°$	$(2L/c)\{1-[1-(n_0/n_c)\exp St]^{1/2}\}(d\ln Z/dt)$
I,L	$n_e = n_c(1-x/L)\exp St$		$(4L/3c)(d\ln Z/dt)(\exp-St)\cos\theta$
$I,$CP	$n_e = n_0(\exp St)$ $\times\{\exp-[2x\ln(n_0/n_c)/L]^{1/2}\}$		$\{(2L/c)(d\ln Z/dt)/[\ln(n_0/n_c)]\}[2(1-\ln2)$ $+\ln(n_0/n_{TP})+(d\ln Z/dt)t]\cos\theta$
I,T	$n_e = n_e(0)\exp St$	$n_e \ll n_c, \theta = 90°$	$(d/2c)(d\ln Z/dt)(n_e/n_c)/(1-n_e/n_c)^{1/2}$
C,E	$n_e = n_0\exp-(x/L+1)$	$\beta^2 \ll 1$	$-32L/15c(\beta^2 d\ln\beta/dt)\cos^5\theta$

ponential density profiles, the shift ratios extracted from Table I are as follows. The hydrodynamic to ionization-front shift ratio is

$$\frac{c_s[\ln(n_0/n_{TP})-1]}{L(d\ln Z/dt)}, \tag{B1}$$

the changing collisionality to ionization-front shift ratio is

$$\frac{16\beta^2 d\ln\beta/dt}{15 d\ln Z/dt}, \tag{B2}$$

and the transverse-probe to normal-probe shift ratio is approximately

$$\frac{\sin\theta}{2} \text{ with } d = 2L\tan\theta, \ n_e = n_{TP} \ll n_c. \tag{B3}$$

From Eqs. (B1) and (B2), ionization front motion will dominate for large scale lengths L and/or ionization rates and also for small values of the collisionality β. Equations (B3), surprisingly, holds for both ionization front motion and hydrodynamic motion. Hence there is no advantage in using transverse probing as a means of isolating ionization-induced shifts. Finally, although exploding foils [45] will yield red shifts in transmission when the peak density falls below critical density, the maximum shift for a realistic exponential profile is only $0.77c_s/c$, almost an order of magnitude less than the blue reflected Doppler shifts that will be present during the overdense phase.

[1] H. M. Milchberg, R. R. Freeman, S. C. Davey, and R. M. More, Phys. Rev. Lett. 61, 2364 (1988).

[2] R. Fedosejevs, R. Ottman, R. Sigel, G. Kuhnle, S. Szatmari, and F. P. Schafer, Appl. Phys. B 50, 79 (1990); R. Fedosejevs, R. Ottman, R. Sigel, G. Kuhnle, S. Szatmari, and F. P. Schafer, Phys. Rev. Lett. 64, 1250 (1990).

[3] M. M. Murnane, H. C. Kapteyn, and R. W. Falcone, Phys. Rev. Lett. 62, 155 (1989); M. M. Murnane, H. C. Kapteyn, M. D. Rosen, and R. W. Falcone, Science 251, 531 (1991).

[4] J.-C. Kieffer, J.-P. Matte, S. Belair, M. Chaker, P. Aude-

bert, H. Pepin, P. Maine, D. Strickland, P. Bado, and G. Mourou, IEEE J. Quantum Electron 25, 2640 (1989).

[5] M. Chaker, J.-C. Kieffer, J. P. Matte, H. Pepin, P. Audebert, P. Maine, D. Strickland, P. Bado, and G. Mourou, Phys. Fluids B 3, 167 (1991).

[6] H. M. Milchberg and R. R. Freeman, Phys. Rev. A 41, 2211 (1990).

[7] O. L. Landen, D. G. Stearns, and E. M. Campbell, Phys. Rev. Lett. 63, 1475 (1989).

[8] H. M. Milchberg and R. R. Freeman, J. Opt. Soc. Am. B 6, 1351 (1989).

[9] T. Engers, W. Fendel, H. Schuler, H. Schulz, and D. von der Linde, Phys. Rev. A **43**, 4564 (1991).

[10] D. Kuhlke, U. Herpers, and D. von der Linde, Appl. Phys. Lett. **50**, 1785 (1987).

[11] D. G. Stearns, O. L. Landen, E. M. Campbell, and J. H. Scofield, Phys. Rev. A **37**, 1684 (1988).

[12] O. R. Wood II, W. T. Silfvast, H. W. K. Tom, W. H. Knox, R. L. Fork, C. H. Brito-Cruz, M. C. Downer, and P. J. Maloney, Appl. Phys. Lett. **53**, 654 (1988).

[13] J. F. Seely, U. Feldman, C. H. Nam, W. Tighe, S. Suckewer, and L. A. Woltz, in *High Intensity Laser-Matter Interactions*, edited by E. M. Campbell and H. Baldis (SPIE, Bellingham, 1988), p. 164.

[14] G. Kuhnle, F. P. Schafer, S. Szatmari, and G. D. Tsakiris, Appl. Phys. B **47**, 361 (1988).

[15] J. A. Cobble, G. A. Kyrala, A. A. Hauer, A. J. Taylor, C. C. Gomez, N. D. Delamater, and G. T. Schappert, Phys. Rev. A **39**, 454 (1989).

[16] S. A. Akhmanov, I. M. Bayanov, V. M. Gordienko, M. S. Dzhidzhoev, S. V. Krayushkin, S. A. Magnitskii, V. T. Platonenko, Yu.V. Ponomarev, A. B. Savel'ev-Trofimov, E. V. Slobodchikov, and A. P. Tarasevich, Kavant. Elektron. (Moscow) **18**, 278 (1991) [Sov. J. Quantum Electron. **21**, 248 (1991)].

[17] H. W. K. Tom and O. R. Wood II, Appl. Phys. Lett. **54**, 517 (1989).

[18] F. Cornolti, P. Mulser, and M. Hahn, Lasers Part. Beams **9**, 465 (1991).

[19] H. M. Milchberg, I. Lyubomirsky, and C. G. Durfee III, Phys. Rev. Lett. **67**, 2654 (1991).

[20] A. Zigler, P. G. Burkhalter, D. J. Nagel, M. D. Rosen, K. Boyer, T. S. Luk, A. McPherson, and C. K. Rhodes, Opt. Lett. **16**, 1261 (1991).

[21] H. C. Kapteyn, M. M. Murnane, A. Szoke, and R. W. Falcone, Opt. Lett. **16**, 490 (1991).

[22] W. L. Kruer, *The Physics of Laser Plasma Interactions* (Addison-Wesley, Redwood City, 1988).

[23] M. D. Rosen, D. W. Phillion, V. C. Rupert, W. C. Mead, W. L. Kruer, J. J. Tomson, H. N. Kornblum, V. W. Slivinsky, G. J. Caporaso, M. J. Boyle, and K. G. Tirsell, Phys. Fluids **22**, 2020 (1979).

[24] K. Estabrook and W. L. Kruer, Phys. Rev. Lett. **40**, 47 (1978).

[25] J. Bloembergen, Opt. Commun. **8**, 285 (1973).

[26] E. Yablonovitch, Phys. Rev. Lett. **32**, 1101 (1974).

[27] W. M. Wood, W. C. Banyai, J. L. Trisnadi, and M. C. Downer, in *Ultrafast Phenomena VII*, edited by C. B. Harris, E. P. Ippen, G. A. Mourou, and A. H. Zewail (Springer-Verlag, New York, 1990), p. 101.

[28] S. C. Wilks, J. M. Dawson, and W. B. Mori, Phys. Rev. Lett. **61**, 337 (1988).

[29] C. J. Joshi, C. E. Clayton, K. Marsh, D. B. Hopkins, A. Sessler, and D. Whittum, IEEE Trans. Plasma Sci. **18**, 814 (1990).

[30] H. C. Kapteyn and M. M. Murnane, J. Opt. Soc. Am. B **8**, 1657 (1991).

[31] W. B. Mori, Phys. Rev. A **44**, 5118 (1991).

[32] T. Dewandre, J. R. Albritton, and E. A. Williams, Phys. Fluids **24**, 528 (1981).

[33] V. I. Semenova, Izv. Vyssh. Uchepn. Zaved. Radiofiz. **10**, 1077 (1971) [Sov. Radiophys. **10**, 599 (1967).

[34] M. Lampe, E. Ott, and J. H. Walker, Phys. Fluids **21**, 42 (1978).

[35] W. M. Wood, G. Focht, and M. C. Downer, Opt. Lett. **13**, 984 (1988).

[36] G. B. Zimmerman and W. L. Kruer, Comments Plasma Phys. Controlled Fusion **2**, 51 (1975).

[37] M. D. Perry, A. Szoke, O. L. Landen, and E. M. Campbell, Phys. Rev. Lett. **60**, 1270 (1988).

[38] V. L. Ginzburg, *The Propagation of EM Waves in Plasmas* (Pergamon, New York, 1970), p. 260.

[39] H. Brysk, P. M. Campbell, and P. Hammerling, Plasma Phys. **17**, 473 (1975); Y. T. Lee and R. M. More, Phys. Fluids **27**, 1273 (1984).

[40] M. D. Perry, O. L. Landen, J. Weston, and R. Ettlebrick, Opt. Lett **14**, 42 (1989).

[41] O. L. Landen, B. T. Vu, D. G. Stearns, and W. E. Alley, in *Short-Pulse High-Intensity Lasers and Applications*, edited by H. A. Baldis (SPIE, Bellingham, 1991), p. 120.

[42] D. Umstadter, X. Liu, J. S. Coe, and C. Y. Chien, in *OSA Proceedings on Short-Wavelength Coherent Radiation*, edited by P. H. Bucksbaum and N. M. Ceglio (Optical Society of America, Washington, DC, 1991), p. 281.

[43] S. C. Wilks, W. L. Kruer, M. Tabak, and A. B. Langdon, Phys. Rev. Lett. (to be published).

[44] M. Born and E. Wolf, *Principles of Optics* (Pergamon, Oxford, 1983).

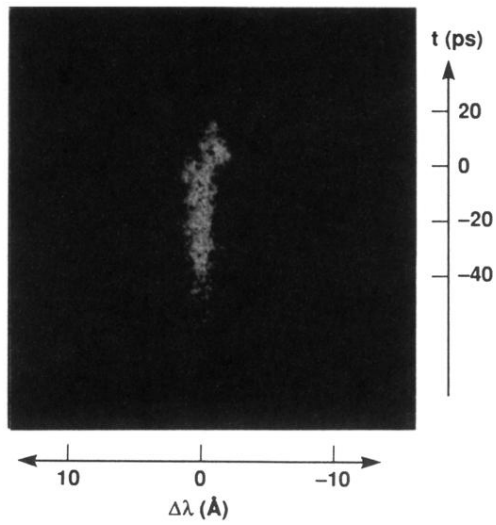[45] H. W. K. Tom, O. R. Wood II, G. D. Aumiller, and M. D. Rosen, in *Ultrafast Phenomena VII* (Ref. [27]), p. 107.

FIG. 6. Streaked spectrum of s-polarized 532-nm, 70-ps probe pulse reflecting at 40° from gold target irradiated at $t = 0$ by 583-nm, 1-ps, 1.5×10^{14}-W cm^{-2} pulse.